PAPER • OPEN ACCESS

Overview of the TCV tokamak experimental programme

To cite this article: H. Reimerdes *et al* 2022 *Nucl. Fusion* **62** 042018

View the article online for updates and enhancements.

Overview of the TCV tokamak experimental programme

H. Reimerdes[1,*] , M. Agostini[2,42], E. Alessi[3], S. Alberti[1], Y. Andrebe[1],
H. Arnichand[1], J. Balbin[4], F. Bagnato[1], M. Baquero-Ruiz[1], M. Bernert[5],
W. Bin[3], P. Blanchard[1], T.C. Blanken[6], J.A. Boedo[7], D. Brida[5],
S. Brunner[1], C. Bogar[8], O. Bogar[8], T. Bolzonella[2], F. Bombarda[9],
F. Bouquey[4], C. Bowman[10], D. Brunetti[3], J. Buermans[11], H. Bufferand[4],
L. Calacci[12], Y. Camenen[13], S. Carli[14], D. Carnevale[12], F. Carpanese[1],
F. Causa[3], J. Cavalier[8], M. Cavedon[5], J.A. Cazabonne[1], J. Cerovsky[8],
R. Chandra[15], A. Chandrarajan Jayalekshmi[1], O. Chellaï[1],
P. Chmielewski[16], D. Choi[1], G. Ciraolo[4], I.G.J. Classen[15], S. Coda[3],
C. Colandrea[1], A. Dal Molin[17], P. David[5], M.R. de Baar[15], J. Decker[1],
W. Dekeyser[14], H. de Oliveira[1], D. Douai[4], M. Dreval[18], M.G. Dunne[5],
B.P. Duval[1], S. Elmore[19], O. Embreus[20], F. Eriksson[20], M. Faitsch[5],
G. Falchetto[4], M. Farnik[8], A. Fasoli[1], N. Fedorczak[4], F. Felici[1], O. Février[1],
O. Ficker[8], A. Fil[10,19], M. Fontana[1], E. Fransson[20], L. Frassinetti[21],
I. Furno[1], D.S. Gahle[19,22], D. Galassi[1], K. Galazka[16], C. Galperti[1],
S. Garavaglia[3], M. Garcia-Munoz[23], B. Geiger[24], M. Giacomin[1], G. Giruzzi[4],
M. Gobbin[2], T. Golfinopoulos[25], T. Goodman[1], S. Gorno[1], G. Granucci[3],
J.P. Graves[1], M. Griener[5], M. Gruca[16], T. Gyergyek[26], R. Haelterman[11],
A. Hakola[27], W. Han[25], T. Happel[5], G. Harrer[28], J.R. Harrison[19],
S. Henderson[19], G.M.D. Hogeweij[15], J.-P. Hogge[1], M. Hoppe[20],
J. Horacek[8], Z. Huang[25], A. Iantchenko[1], P. Innocente[2],
K. Insulander Björk[20], C. Ionita-Schrittweiser[29], H. Isliker[30], A. Jardin[31],
R.J.E. Jaspers[6], R. Karimov[1], A.N. Karpushov[1], Y. Kazakov[11], M. Komm[8],
M. Kong[1,19], J. Kovacic[26], O. Krutkin[1], O. Kudlacek[5], U. Kumar[1],
R. Kwiatkowski[32], B. Labit[1], L. Laguardia[3], J.T. Lammers[6], E. Laribi[4],
E. Laszynska[16], A. Lazaros[33], O. Linder[5], B. Linehan[25], B. Lipschultz[10],
X. Llobet[1], J. Loizu[1], T. Lunt[5], E. Macusova[8], Y. Marandet[13],
M. Maraschek[5], G. Marceca[1], C. Marchetto[3], S. Marchioni[1],
E.S. Marmar[25], Y. Martin[1], L. Martinelli[1], F. Matos[5], R. Maurizio[1,42],
M.-L. Mayoral[19], D. Mazon[4], V. Menkovski[6], A. Merle[1], G. Merlo[34],
H. Meyer[19], K. Mikszuta-Michalik[16], P.A. Molina Cabrera[1,25], J. Morales[4],
J.-M. Moret[1], A. Moro[3], D. Moulton[19], H. Muhammed[19], O. Myatra[10],
D. Mykytchuk[1], F. Napoli[9], R.D. Nem[35], A.H. Nielsen[35], M. Nocente[17],
S. Nowak[3], N. Offeddu[1], J. Olsen[35], F.P. Orsitto[36], O. Pan[5], G. Papp[5],
A. Pau[1], A. Perek[15], F. Pesamosca[1], Y. Peysson[4], L. Pigatto[2], C. Piron[2],
M. Poradzinski[16], L. Porte[1], T. Pütterich[5], M. Rabinski[32], H. Raj[1],
J.J. Rasmussen[35], G.A. Rattá[37], T. Ravensbergen[6,15], D. Ricci[3], P. Ricci[1],

N. Rispoli[3]**, F. Riva**[19]**, J.F. Rivero-Rodriguez**[23]**, M. Salewski**[35]**, O. Sauter**[1]**,
B.S. Schmidt**[35]**, R. Schrittweiser**[29]**, S. Sharapov**[19]**, U.A. Sheikh**[1]**,
B. Sieglin**[5]**, M. Silva**[1]**, A. Smolders**[1,14]**, A. Snicker**[27]**, C. Sozzi**[3]**,
M. Spolaore**[2]**, A. Stagni**[1,38]**, L. Stipani**[1]**, G. Sun**[1]**, T. Tala**[27]**, P. Tamain**[4]**,
K. Tanaka**[39]**, A. Tema Biwole**[1]**, D. Terranova**[2]**, J.L. Terry**[25]**, D. Testa**[1]**,
C. Theiler**[1]**, A. Thornton**[19]**, A. Thrysøe**[35]**, H. Torreblanca**[1]**, C.K. Tsui**[1,7]**,
D. Vaccaro**[1,40]**, M. Vallar**[1]**, M. van Berkel**[15]**, D. Van Eester**[11]**,
R.J.R. van Kampen**[6,15]**, S. Van Mulders**[1]**, K. Verhaegh**[10]**, T. Verhaeghe**[11]**,
N. Vianello**[2]**, F. Villone**[36]**, E. Viezzer**[23]**, B. Vincent**[1]**, I. Voitsekhovitch**[19]**,
N.M.T. Vu**[1]**, N. Walkden**[19]**, T. Wauters**[11]**, H. Weisen**[1]**, N. Wendler**[16]**,
M. Wensing**[1]**, F. Widmer**[13]**, S. Wiesen**[41]**, M. Wischmeier**[5]**, T.A. Wijkamp**[6,15]**,
D. Wünderlich**[5]**, C. Wüthrich**[1]**, V. Yanovskiy**[8]**, J. Zebrowski**[27] **and
the EUROfusion MST1 Team**[a]

[1] Ecole Polytechnique Fédérale de Lausanne (EPFL), Swiss Plasma Center (SPC), Lausanne, Switzerland
[2] Consorzio RFX, Padova, Italy
[3] Istituto per la Scienza e Tecnologia dei Plasmi ISTP-CNR, Milano, Italy
[4] CEA, IRFM, Saint Paul-Lez-Durance Cedex, France
[5] Max Planck Institute for Plasma Physics, Garching, Germany
[6] Eindhoven University of Technology, Eindhoven, Netherlands
[7] Center for Energy Research (CER), University of California-San Diego (UCSD), La Jolla, CA, United States of America
[8] Institute of Plasma Physics of the CAS, Prague, Czech Republic
[9] Unità Tecnica Fusione, ENEA, Frascati, Italy
[10] York Plasma Institute, University of York, Heslington, York, United Kingdom of Great Britain and Northern Ireland
[11] Laboratory for Plasma Physics, LPP-ERM/KMS, Brussels, Belgium
[12] University of Rome Tor Vergata, Rome, Italy
[13] CNRS, Aix-Marseille Univ., Marseille, France
[14] KU Leuven, Department of Mechanical Engineering, Leuven, Belgium
[15] DIFFER-Dutch Institute for Fundamental Energy Research, Eindhoven, Netherlands
[16] Institute of Plasma Physics and Laser Microfusion (IPPLM), Warsaw, Poland
[17] Universita' di Milano-Bicocca, Milano, Italy
[18] Institute of Plasma Physics of the NSC KIPT, Kharkov, Ukraine
[19] CCFE, Culham Science Centre, Abingdon, Oxon, United Kingdom of Great Britain and Northern Ireland
[20] Chalmers University of Technology, Gothenburg, Sweden
[21] KTH Royal Institute of Technology, Stockholm, Sweden
[22] SUPA, University of Strathclyde, Glasgow, United Kingdom of Great Britain and Northern Ireland
[23] University of Seville, Spain
[24] University of Wisconsin - Madison, Madison, WI, United States of America
[25] Plasma Science and Fusion Center, Massachusetts Institute of Technology, Cambridge, MA, United States of America
[26] Jožef Stefan Institute, Ljubljana, Slovenia
[27] VTT, Espoo, Finland
[28] Institute of Applied Physics, Fusion@ÖAW, T.U. Wien, Vienna, Austria
[29] Institut für Ionenphysik und Angewandte Physik, Universität Innsbruck, Innsbruck, Austria
[30] Aristotle University of Thessaloniki, Thessaloniki, Greece
[31] Institute of Nuclear Physics Polish Academy of Sciences (IFJ PAN), Krakow, Poland
[32] National Centre for Nuclear Research (NCBJ), Otwock, Poland
[33] Department of Physics, National and Kapodistrian University of Athens, Athens, Greece
[34] University of Texas at Austin, Austin, TX, United States of America
[35] Department of Physics, Technical University of Denmark, Kgs. Lyngby, Denmark
[36] University of Napoli 'Federico II', Consorzio CREATE, Napoli, Italy
[37] Laboratorio Nacional de Fusión, CIEMAT, Madrid, Spain
[38] Politecnico di Milano, Milan, Italy
[39] National Institute for Fusion Science, National Institutes of Natural Sciences, Toki, Gifu, Japan
[40] Department of Economics, Engineering, Society and Business Organization (DEIm), University of Tuscia, Viterbo, Italy

[41] Forschungszentrum Jülich GmbH, Institut für Energie- und Klimaforschung—Plasmaphysik, Jülich, Germany
[42] Oak Ridge Associated Universities (ORAU), Oak Ridge, TN, United States of America

E-mail: holger.reimerdes@epfl.ch

CrossMark

Abstract

The tokamak à configuration variable (TCV) continues to leverage its unique shaping capabilities, flexible heating systems and modern control system to address critical issues in preparation for ITER and a fusion power plant. For the 2019–20 campaign its configurational flexibility has been enhanced with the installation of removable divertor gas baffles, its diagnostic capabilities with an extensive set of upgrades and its heating systems with new dual frequency gyrotrons. The gas baffles reduce coupling between the divertor and the main chamber and allow for detailed investigations on the role of fuelling in general and, together with upgraded boundary diagnostics, test divertor and edge models in particular. The increased heating capabilities broaden the operational regime to include $T_e/T_i \sim 1$ and have stimulated refocussing studies from L-mode to H-mode across a range of research topics. ITER baseline parameters were reached in type-I ELMy H-modes and alternative regimes with 'small' (or no) ELMs explored. Most prominently, negative triangularity was investigated in detail and confirmed as an attractive scenario with H-mode level core confinement but an L-mode edge. Emphasis was also placed on control, where an increased number of observers, actuators and control solutions became available and are now integrated into a generic control framework as will be needed in future devices. The quantity and quality of results of the 2019–20 TCV campaign are a testament to its successful integration within the European research effort alongside a vibrant domestic programme and international collaborations.

Keywords: nuclear fusion, tokamak, TCV, EUROfusion

(Some figures may appear in colour only in the online journal)

1. Introduction

The tokamak à configuration variable (TCV) [1] is a carbon walled, medium sized (major radius $R_0 = 0.88$ m, magnetic field $B_0 \leqslant 1.5$ T), conventional aspect ratio ($A \approx 4$) tokamak with unique shaping capabilities. Together with flexible heating systems for electrons and ions, a steadily growing number of diagnostics and a modern control system, it continues to address critical issues in preparation for ITER and a fusion power plant. For the 2019–20 campaign its configurational flexibility has been enhanced with the installation of divertor baffles, its diagnostic capabilities with numerous upgrades and its heating systems with new gyrotrons. These recent enhancements are part of a greater facility upgrade that commenced in 2015 [2] in contribution to the EU strategy to solve the DEMO exhaust problem [3]. Experiments are performed in part by topical teams, under the auspices of the EUROfusion medium-size tokamak programme and local teams at the Swiss Plasma Center together with international collaborators.

Auxiliary heating is provided by a neutral beam injection (NBI) system [4] and X2 and X3 electron cyclotron resonance heating (ECRH) systems. An improved acceleration grid for the NBI system, with reduced beam divergence [5] and, hence, lower power losses in the duct together with an improved duct cooling [6] permitted a 2.5× increase in injected energy with injected powers up to 1.3 MW. In addition, 1.0 MW NBI operation in hydrogen has been demonstrated. The legacy ECRH system of 1.4 MW from two 83 GHz gyrotrons (X2) and 0.9 MW from two 118 GHz gyrotrons (X3) was enhanced by two 1.0 MW dual frequency (84/126 GHZ) gyrotrons for X2 or X3 heating [7]. The first dual-frequency gyrotron started operation in 2019 and performed as designed, validating the numerical models used in its development [8]. A second unit has recently attained the same performance and is being integrated into the ECRH waveguide system for plasma operation.

The most conspicuous upgrade was the installation of a first set of removable gas baffles for the 2019 experimental campaign. Its effect on the neutral distribution is described in section 2. The baffles had a large impact on the TCV edge and divertor programme, summarised in section 3. With more auxiliary heating, H-mode studies towards a better understanding of the ITER baseline scenario gained prominence, section 4. As type-I ELMs associated with the baseline scenario are of great concern for the safety of the ITER divertor, and certainly

unacceptable in a reactor, a significant part of the experimental programme was dedicated to research in alternative scenarios, discussed in section 5. Several specific issues of concern for ITER operation are addressed in section 6. Section 7 gives an overview of TCV's contributions to real-time control of interest for ITER and beyond, before some conclusions in section 8.

2. Divertor upgrade

The divertor upgrade is centred around the installation of removable gas baffles that partially separate the vessel into main and divertor chambers, figure 1(*a*). The baffles primarily seek to increase the divertor neutral pressure and thereby facilitate extrapolation to future devices, such as ITER that will rely upon a high divertor neutral pressure. The divertor closure of a first set of baffles was optimised for a large neutral compression in a conventional, single-null divertor, figure 1(*b*), using the edge transport code SOLPS-ITER, which employs a fluid description of the plasma coupled with kinetic neutrals [2]. The baffles consist of graphite tiles that replace standard wall protection tiles, requiring only short manned entries for installation and removal. The first set of baffles was installed for the 2019 experimental campaign [9]. The baffles were complemented with new port protection tiles that shadow magnetic field lines, shielding the lower lateral port openings from direct contact with plasma. These are independent of the baffles and increase the configurational flexibility for both baffled and un-baffled configurations, figures 1(*c*)–(*e*). Divertor diagnostics were also upgraded with additional wall mounted Langmuir probes [10] and an additional IR thermography system for complete divertor chamber coverage. A new, long-throw reciprocating divertor probe array (RDPA) extends measurements into the divertor volume [11], where new divertor Thomson scattering chords, equipped with narrow filters, are now able to measure electron temperatures down to 1 eV [12]. Radiation diagnostics are greatly enhanced with a new tomography camera array each housing sensitive foil bolometers, and separate AXUV and soft x-ray (SXR) diode arrays to reconstruct radiation profiles in the divertor and the main chamber. The system is complemented by a tangentially viewing, multi camera spectral imaging system, MANTIS [13], and wider coverage divertor spectroscopy chords (DSS) [14]. Probe turbulence measurements are augmented with a new gas puff imaging (GPI) system in the proximity of the *X*-point.

Experimentally, Ohmically heated diverted discharges, figure 1(*b*), qualitatively confirm SOLPS-ITER predictions [15] with up to a 5× increase in divertor neutral pressure [9, 16], figure 2. The concurrently predicted decrease of the main chamber neutral density is, as yet, unconfirmed as the associated pressure is below the noise level of the current TCV baratron of several millipascal. A trend towards a higher ratio of separatrix density, $n_{e,sep}$, and line averaged density, $\langle n_e \rangle$, in the baffled configuration, however, indicates a reduction in core ionisation and, hence, a lower main chamber neutral density [17]. Optional fuelling into the divertor or the main chamber can disentangle the effects of fuelling rate, divertor and/or main chamber neutral pressure, $p_{n,div/main}$, and plasma density, n_e. These new device capabilities provided by the baffles, were extensively used for studies of the divertor and the plasma edge, discussed in section 3, and contributed to several other aspects of TCV's scientific programme.

Scanning the plasma plugging by displacing the *X*-point with respect to the baffles, indicates that the installed divertor closure is close to optimal [16]. SOLEDGE2D-Eirene calculations with a more refined main chamber plasma–wall interaction (PWI) model than SOLPS-ITER suggest that increasing the closure may further increase the neutral compression [18] guiding the design of future baffles.

The baffles were removed in early 2020, restoring TCV's full shaping flexibility, but will be re-installed for dedicated future campaigns. In addition, a second baffle set with less closure, better suited for snowflake configurations, see section 3.2, is being procured and will be installed in 2021. This will be followed in 2022 by a third combination of inner and outer baffles with greater closure than the initial set reported herein.

3. Edge physics

Plasma exhaust, and its compatibility with high core performance, is one of the main challenges on the way to fusion energy. The challenge is set by the width of the scrape-off layer (SOL) with solutions hinging on achievable separatrix densities and the tolerable seed impurity concentrations. Since the conditions of future high-performance devices, with higher heat fluxes, larger dimensions and greater magnetic fields, cannot be achieved in today's experiments, the development of predictive edge modelling capability is mandatory. TCV contributes by testing edge models, including those used in the design of the ITER divertor [19] and by exploring alternative configurations to the conventional single-null divertor to improve future reactor designs [20, 21].

3.1. Plasma exhaust in the conventional divertor

The effect of the neutral pressure in a conventional single-null divertor, figure 1(*b*), is investigated by comparing identically programed density ramp discharges in baffled and un-baffled configurations. These discharges are performed in *reverse field*, where the magnetic field is directed in the unfavourable direction for H-mode access to remain in L-mode. L-mode plasmas facilitate tests of divertor models as they are easier to diagnose and plasma parameters are generally more stationary. Measurements with target Langmuir probes and the novel RDPA diagnostic show that, as predicted, increasing $p_{n,div}$ in the baffled divertor leads to a cooler and denser divertor plasma for the same core density [22]. Ion flux measurements with the RDPA also reveal a stronger ionisation source in the baffled divertor. As a result, and again as predicted, detachment detected by its characteristic target particle flux roll-over, figure 3(*a*), and a displacement of the CIII emission front towards the *X*-point, figure 3(*b*), commences at 20%–30% lower $\langle n_e \rangle$ [16]. Experiments using main chamber fuelling provide further evidence that the onset of detachment is primarily determined by $p_{n,div}$ rather than n_e.
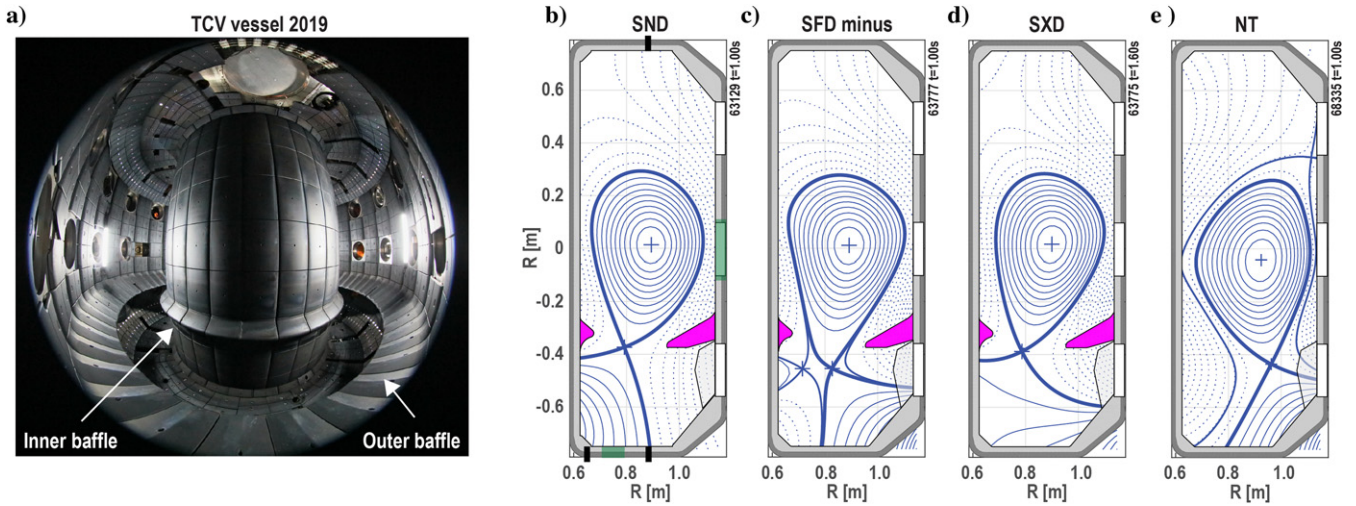
Figure 1. (*a*) Fisheye lens photograph of the inside of the baffled TCV vessel (Photo: Alain Herzog/EPFL) and poloidal cross sections of (*b*) single-null diverted, (*c*) snowflake-minus and (*d*) super-X configurations in TCV with baffles (magenta) and (*e*) a diverted negative-triangularity configuration employing the port protection tiles (light grey). Gas fuelling (black) and neutral pressure measurement locations (green) are indicated in (*b*). Reproduced courtesy of IAEA. Figure from [9]. © 2021 EURATOM.
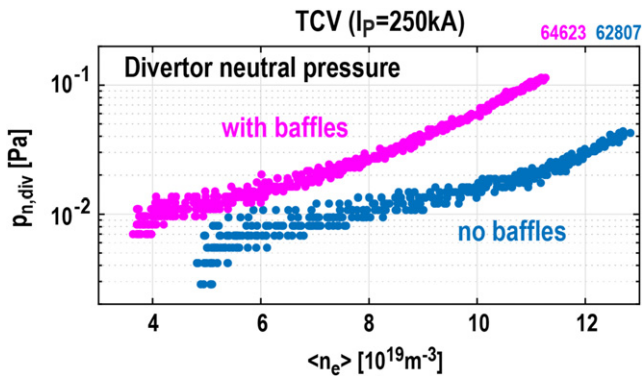

Figure 2. Baratron measurements of the neutral pressure in the divertor in Ohmic density ramps with (magenta) and without the baffles (blue). Reproduced courtesy of IAEA. Figure from [9]. © 2021 EURATOM.

Efforts to test drift models in the SOLPS-ITER code predicted an electric potential well and altered drift patterns in reverse field discharges with extremely low plasma temperatures in the divertor [23]. RDPA measurements in baffled discharges at sufficiently high density and, hence, sufficiently low plasma temperature, subsequently confirmed the presence of such a well [24]. Target current measurements show that, in the cold TCV divertor, more easily accessible with baffles, SOL currents are dominated by Pfirsch–Schlüter currents [24]. These measurements employed a plasma current of 190 kA, the highest value for reliable Ohmic L-mode operation, and both field directions. Measured peaks in the target current, their directions and dependence on field directions and density, are found in qualitative agreement with SOLPS-ITER calculations. A high-fidelity test of SOLPS-ITER was attempted for a density ramp discharge in reverse field and with a somewhat higher current of 250 kA [25]. Cross-field diffusivities were set to match the T_e and n_e profiles measured by Thomson scattering well above the *X*-point. The model
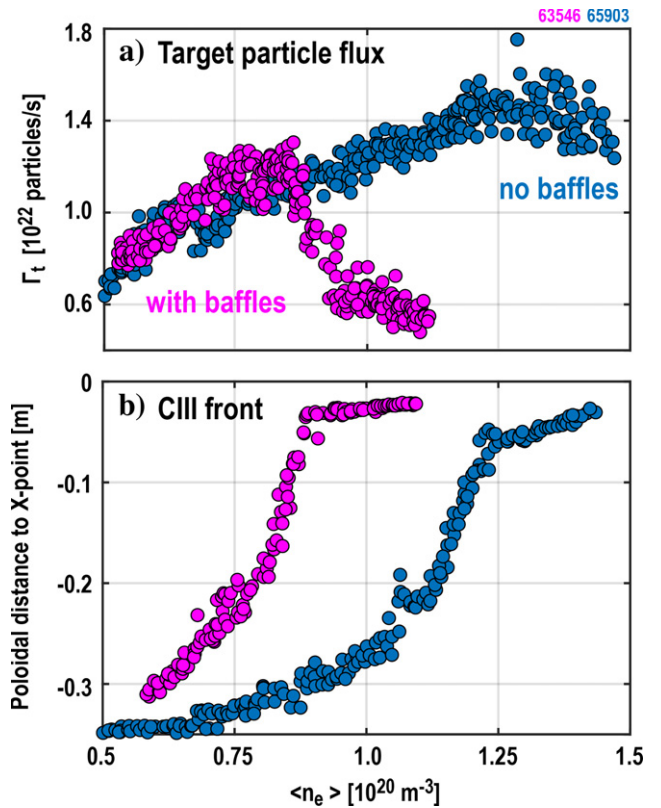

Figure 3. Density dependence of (*a*) the particle fluxes at the outer target measured with Langmuir probes and (*b*) the CIII (465 nm) emission front position measured with MANTIS in Ohmic discharges with (magenta) and without the baffles (blue). Reprinted from [16], Copyright (2021), with permission from Elsevier. CC BY-NC-ND 4.0.

then reasonably describes T_e and n_e below the *X*-point, measured with the reciprocating probe (RPTCV), and near the outer target, by the new divertor Thomson chords, albeit with somewhat broader than predicted profiles. The model, however, clearly overpredicts the target plasma density and

underpredicts its temperature. The model, also, concurrently overpredicts the divertor neutral pressure (by approximately a factor 4). The identified discrepancies will guide further refinements in the model and spur diagnostic developments. One recent question, for example, is the accuracy of the description of molecular-activated recombination (MAR) that, according to a recent spectroscopic investigation, can provide a significant volumetric particle sink in TCV discharges [26, 27].

Detachment was also obtained with nitrogen seeding in reverse field, Ohmic, L-mode discharges [28]. A sufficiently high seeding rate led to the detachment at both targets and the formation of a stable radiator around the *X*-point. Measurements with TCV's gold-foil bolometer system, with 64 intersecting lines of sight, indicate that up to 80% of the power crossing the last closed flux surface (LCFS) into the SOL can thus be radiated. While nitrogen seeding generally reduced the energy confinement time, this reduction is only a marginal effect at higher plasma density, indicative of a lower level of nitrogen penetration into the core plasma and, yet again, consistent with SOLPS-ITER simulations [29].

3.2. Plasma exhaust in alternative divertor configurations

Inspired by the MAST-Upgrade design [30], and motivated by recent SOLPS-ITER simulations that explain the absence of advantageous effects of a larger target radius in previous TCV experiments with a varying angle between the divertor leg and the target surface and poor neutral trapping [31], detailed investigations were conducted on TCV's *super-X divertor* configuration [32], figure 1(*d*). Specific configurations designed to disentangle the effects of a large target radius, R_t, and the angle between the divertor leg and the target surface, and employing the divertor baffles and a newly installed gas valve to fuel into the private flux region, figure 4(*a*), confirm the predicted dependence of the detachment onset on this angle and demonstrate a reduction in the detachment threshold with larger R_t, figure 4(*b*). This reduction, however, remains weaker than predicted [31] for a strongly baffled divertor. Target measurements with Langmuir probes reveal that, while the electron temperature decreases with larger R_t, the electron density does not increase as expected, reminiscent of the discrepancies identified for the single-null divertor, section 3.1.

Other investigations addressed the *snowflake minus* configuration, figure 1(*c*), where a secondary *X*-point in the divertor splits one side of the SOL into distinct divertor legs with consequences for the power distribution to the targets and the radiation volume. In attached conditions, upstream profiles, from reciprocating probe measurements, remain independent of the divertor configuration. Probe measurements at the entrance of the low-field side snowflake minus divertor, a configuration that attracted attention due to its unexpectedly strong broadening of the SOL at the secondary *X*-point [33], reveal large pressure drops that depend on the position of the secondary *X*-point and the drift direction and highlight the dominant role of parallel convection and $E \times B$ drifts in the power distribution to the targets [34]. Operating the snowflake minus in the baffled TCV divertor revealed significant particle fluxes

to the top of the baffle, indicative of divertor over-closure. This hypothesis is supported by experiments on a variant of the snowflake minus, where only the outer divertor is baffled, which achieved a higher divertor neutral pressure than the fully baffled snowflake [35]. This will be further tested with the next combination of baffles foreseen for 2021.

3.3. H-mode/ELMs

Power exhaust studies were extended to type-I ELMy H-modes at 170 kA ($q_{95} = 4.6$) and with 700 kW of NBI heating well above the NBI power of ~450 kW needed to access H-mode [16]. The addition of the divertor baffles decreases the peak electron temperature at the outer target between ELMs from ~5 eV to ~3 eV. Lower divertor temperatures in the baffled divertor are supported by measurements of CIII emission, which is located farther from the target in baffled discharges. Seeding of nitrogen is effective in further cooling the divertor between ELMs as seen by a three-fold decrease in the target particle flux and a CIII emission front that recedes towards the *X*-point with baffles, figure 5(*b*). There are, in particular, no indications of a bi-furcation in either case. However, even with strong seeding, ELMs are able to re-attach the plasma divertor legs, figure 5(*a*).

3.4. SOL width/turbulence and blobs

The width of the heat carrying plasma channel of the SOL, λ_q, and its extrapolation to future devices, is key in determining the magnitude of the heat exhaust challenge. Its value generally decreases in H-mode, relevant for most current reactor scenarios, thus magnifying this challenge. Its L-mode scaling remains important as it determines mitigation requirements during the start-up and landing phases of the discharge.

The extensive database of SOL width measurements in TCV L-modes [36], together with a cross-machine database of λ_q [37] spanning more than an order of magnitude, is found to be well described by an analytical model based on turbulent cross-field transport driven by resistive ballooning modes competing with convective parallel transport [38]. A larger experimental spread seen on all devices is attributed to experimental conditions that extend beyond the sheath-limited regime and geometric modifications, such as plasma triangularity, known to affect the ballooning stability, that are, as yet, ignored by the model. Shaping effects are, however, included in the GBS code [39]. A rigorous validation exercise employing reciprocating probe fluctuation measurements in TCV discharges with circular, elongated and (negative) triangular cross sections showed that the shaping model implemented in GBS improves the description of SOL turbulence [40].

In H-mode, the TCV inter-ELM SOL is typically found 2 times smaller than in L-mode, similar to observations in other devices [41], but also 2–3 times smaller than for H-modes in other devices for the same value of poloidal field (PF) [42], suggesting that a scaling solely based on B_{pol} does not capture all key dependencies. The TCV measurements, however, agree with cross-machine scalings [43] that include terms for the toroidal field, q_{95} and heating power.
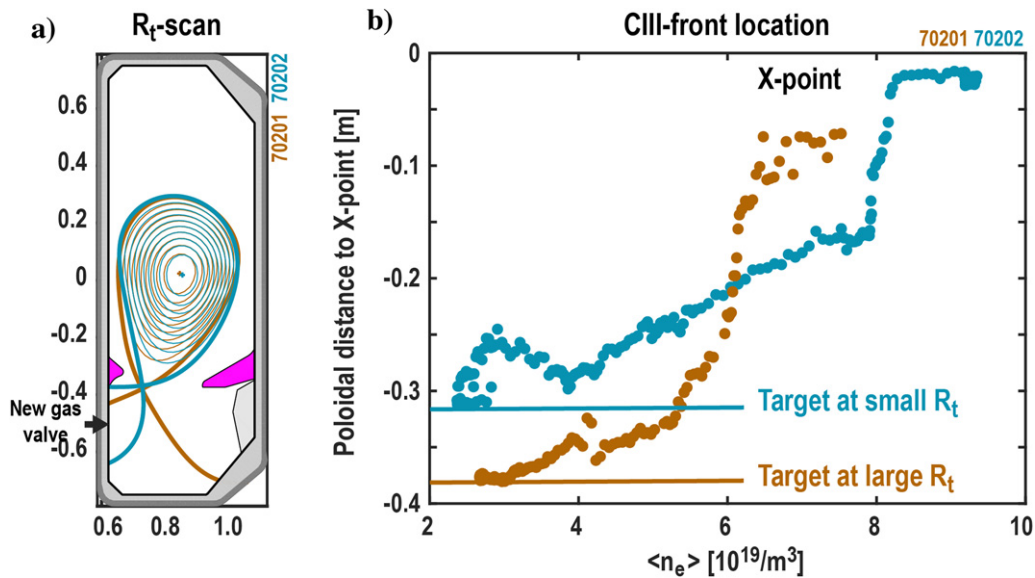
Figure 4. (*a*) Poloidal cross sections of two discharges with similar core shaping, but small (blue) and large (brown) outer target radii and (*b*) density dependence of the poloidal distance of the CIII (465 nm) emission front measured with MANTIS. Reproduced with permission from [32].
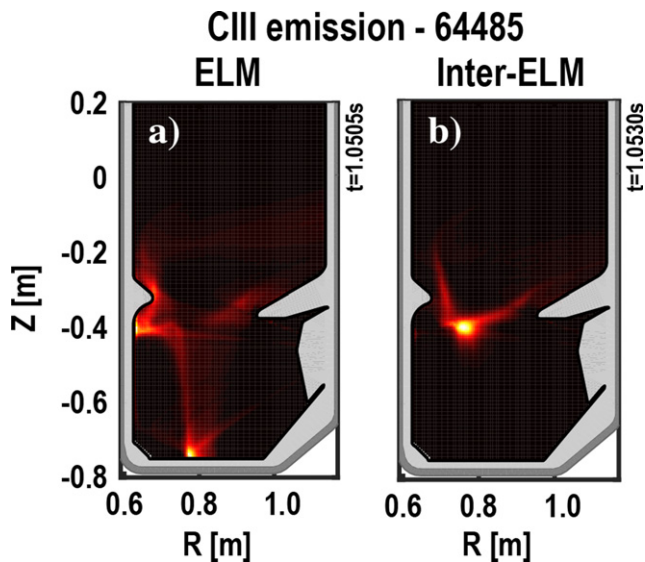

Figure 5. CIII emission (465 nm) obtained from inverted MANTIS images during an ELM (*a*) and in-between ELMs (*b*) in nitrogen seeded discharges with the divertor baffles. Reprinted from [16], Copyright (2021), with permission from Elsevier. CC BY-NC-ND 4.0.

At sufficiently high density, the SOL is generally observed to broaden, with a distinct second, longer, fall-off length in the plasma density emerging—a process referred to as *shoulder formation*. While the density shoulder does little to alleviate heat loads in the divertor, it is feared it may increase main chamber recycling and erosion, with consequences for particle control, impurity influx and lifetime of the first wall in future devices. Repetition of L-mode discharges that clearly displayed a density shoulder in the un-baffled divertor, showed no such evidence in the baffled divertor, although divertor detachment starts at lower plasma density, providing further evidence that SOL collisionality is not the sole determining criterion [44]. Since baffles are expected to operate with a

decreased main chamber neutral density, this behaviour indicates an important effect of neutrals on SOL transport, for example via suppressing zonal flows that stabilise anomalous transport [45] or blob fuelling [46]. Further support for the importance of the main chamber neutral density is obtained from an inner gap scan in the un-baffled divertor [44], with a smaller gap resulting in a more pronounced density shoulder, consistent with a strong, reinforcing, role of main chamber recycling and, hence, neutral pressure.

The characterisation of the SOL turbulence in TCV was extended to H-mode [47]. In the analysed high triangularity ($\delta = 0.5$), low current ($I_P = 180$ kA), H-mode scenario with 1 MW of NBI heating, the inter-ELM density profiles exhibit a broadening with sufficiently strong fuelling and, hence, divertor neutral pressure, $p_{n,div}$, similar to observations on ASDEX-Upgrade and JET. This broadening is accompanied by an increased blob frequency, as detected by Langmuir probes at the outboard midplane wall. Contrary to observations in L-mode, the broadening also prevails for a baffled divertor. The broadening of the upstream density profile is, however, not observed when a dissipative divertor is formed using nitrogen seeding rather than deuterium fuelling.

4. H-mode physics

H-mode studies, as the confinement regime foreseen for ITER, are a prominent part of the TCV programme. The addition of the NBI for auxiliary heating has less constraints on electron density and temperature than TCV's well-established EC heating schemes and heats ions, in addition to electrons, that was found to greatly enhance the H-mode operating range.

4.1. L–H power threshold

The L–H threshold, P_{LH}, remains a critical issue for ITER and for a reactor as it determines the minimum required installed
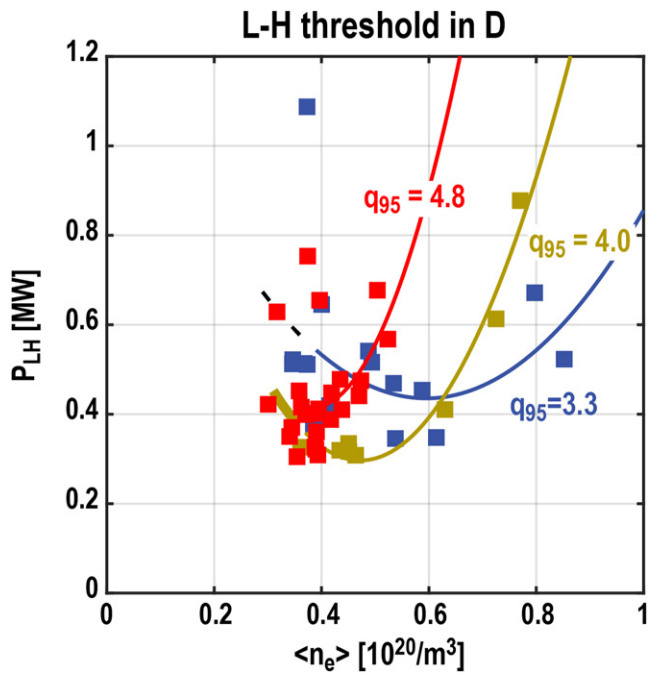
Figure 6. Density dependence of the H-mode threshold in NBI heated discharges at various values of the safety factor.

Figure 7. Measured (*a*) electron temperature and (*b*) density pedestal in unfueled, $P_{NBI} = 1$ MW discharge with (magenta) and without (cyan) baffles.

auxiliary heating power, and, neglecting hysteresis, also sets the minimum power that must be successfully exhausted in a divertor during H-mode operation. Current extrapolations are based on empirical scaling laws with 'hidden parameters' that were experimentally observed to affect the measured value.

The NBI system allows strong decoupling between heating and plasma current that led to the discovery of a strongly increasing current (or unfavourable q_{95}) dependence of P_{LH} that increases with density [48], figure 6. This is not included in the present ITPA scaling [49] where good agreement is only obtained for $q_{95} < 3.5$ or at a plasma density close to the minimum required to enter H-mode that, ironically, may be the least favourable operational position to enter H-mode with regard to ELM heat loads. Revisiting the isotope and charge number dependence with experiments in D, H and He resulted in good agreement with the ITPA scaling, again provided that q_{95} is sufficiently low. Adding small concentrations of D to H plasmas showed, however, a rapid decrease of the L–H threshold suggesting doping of H-plasmas as an option to lower P_{LH} in the pre-nuclear phase of ITER.

4.2. H-mode pedestal

Particular attention was dedicated to the pedestal in type-I ELMy H-modes, where the baffles were used to decouple the roles of main chamber and divertor neutral pressures, $p_{n,main}$ and $p_{n,div}$, in the pedestal structure. Fuelling and, thereby, a higher neutral pressure, generally degrades the pedestal pressure, $p_{e,ped}$, through a degradation of the temperature pedestal, while the density pedestal height remains approximately constant, consistent with previous findings [50]
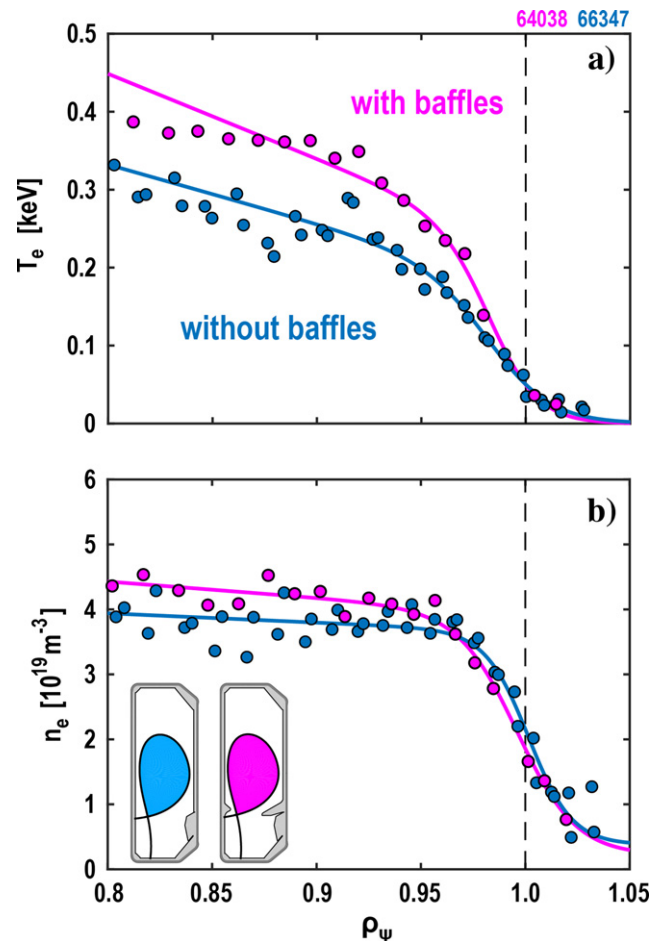
that linked this degradation to an outward shift of the density profile. This outward shift and the related pedestal degradation are, however, found to be considerably more benign in the baffled divertor, presumably due to a weaker increase of $p_{n,main}$, leading to a significantly higher $T_{e,ped}$ and, hence, higher $p_{e,ped}$ at high divertor neutral pressure, $p_{n,div}$, figure 7, [51]. In this way, high fuelling rates, together with nitrogen seeding into the baffled divertor, resulted in an up to three-fold increase in the radiated power without significant core confinement degradation, figure 8. This improved performance was also observed across a range of target radii, R_t, highlighting alternative divertors' weak effect on pedestal and core properties.

4.3. Core confinement

In a continued effort to extrapolate ELMy H-mode performance to the ITER baseline (IBL) scenario, NBI and X3 heated H-modes succeeded in matching the ITER targets of $\kappa = 1.8$, $\delta = 0.5$, $\beta_N = 1.8$ and $q_{95} = 3.0$ whilst retaining good confinement ($H_{98y2} \sim 1$) [52]. The Greenwald fraction reached 0.65, which is still lower than the IBL target, but sufficient for EC absorption at the third harmonic (X3) to become unreliable. Since EC heating with X3 is effective in preventing, or
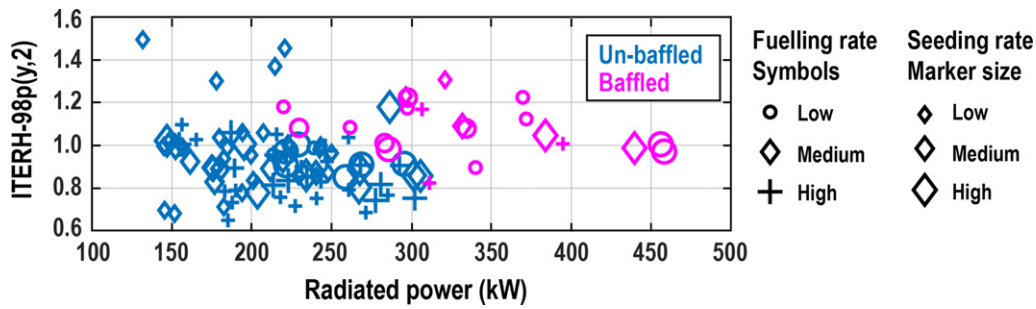
Figure 8. ITERH-98(y, 2) as a function of the total radiated power for various fuelling rates (symbols) and nitrogen seeding rates (marker size) with and without baffles (magenta and cyan, respectively). Reproduced from [51]. CC BY 4.0.

delaying, low m/n (usually 2/1) MHD, ELM triggered neoclassical tearing modes (NTMs) were only avoided by reducing I_P and, hence, the density, with a stationary demonstration of the scenario at $q_{95} = 3.6$. The plasma shape of the TCV IBL discharge was chosen to match a corresponding experiment in ASDEX-Upgrade. Integrated modelling of TCV's IBL discharges predicted the observed heat and particle transport, with dominant ITG modes. It also shows that the observed density peaking is sustained by core NBI fuelling and turbulent transport.

4.4. Density limit

ITER and other future high-performance devices need to operate at densities close to the density limit for high fusion power and divertor protection. The H-mode density limit has therefore been studied in TCV in newly developed NBI-heated scenarios at $I_P = 170$ kA and 100 kA, corresponding to $q_{95} = 3.7$ and 6.2, respectively. In both scenarios, a density ramp follows the characteristic phases also observed in other devices (e.g. on ASDEX Upgrade [53] [54]). At sufficiently high core density, the temperature pedestal starts to erode, and confinement to degrade, which is ultimately followed by an H–L back transition and the formation of a strongly radiating region at the X-point generally associated with an MARFE (*multifaceted asymmetric radiation from the edge*). A further density increase leads to strong edge cooling, an upward displacement of the MARFE from the X-point along the high-field side edge and, eventually, macroscopic MHD leading to a disruption at a line averaged density close to the Greenwald limit. The evolution through these phases is more gradual in the baffled divertor and occurs at lower edge density than in the un-baffled divertor, consistent with higher divertor dissipation (see section 3.1). Experiments demonstrated that additional NBI heating power is effective in counteracting the upward MARFE displacement and, therefore, qualified NBI as a valuable actuator for feedback-controlled operation near the density limit (see section 7.4).

5. Alternative ELM-free regimes

While H-mode confinement is key for reactor designs with realistic dimensions, the cyclical heat and particle loads of type-I ELMs are prohibitive and robust mitigation techniques or alternative scenarios must be found.

5.1. Small ELM regime

The small ELM regime, developed on ASDEX-Upgrade and TCV [55] and also referred to as *quasi-coherent exhaust* regime [56], greatly reduces the transient power and particle loads associated with type-I ELMs. This regime requires high triangularity, a close to double-null diverted configuration, and steady gas fuelling where small ELMs gradually replace large ELMs at sufficiently high separatrix density [57]. The small ELM regime could also be accessed in the baffled TCV divertor, where it requires a substantially increased divertor fuelling rate. The regime's operational window was extended down to $q_{95} \sim 3.7$, albeit only at reduced toroidal field [58]. First attempts at nitrogen seeding in the baffled divertor showed no significant detrimental effect on core confinement, reminiscent of the observations in type-I ELMy regimes, section 4.2, although a comparison with the un-baffled divertor is still pending.

A comparison of the pedestal dynamics of the small ELM regime with type-I ELMs was performed using a novel short-pulse reflectometer [59]. The reflectometer takes advantage of new advances in hardware, particularly GHz-range arbitrary waveform generators and vector-network-analyser extension modules. Shifting the reflectometry paradigm from the conventional frequency domain to the time domain, the time of flight of nanosecond-scale pulses is measured directly, and fast scans of the wave-train frequency can resolve the entire density profile on a microsecond-scale [60]. The instrument measures fast changes in pedestal density profiles with high spatio-temporal resolution (mm and μs). The small-ELM scenario is found to feature a $\sim$25–35 kHz quasi-coherent density fluctuation near the separatrix $\rho_\psi \sim 0.993$–1.05 not observed during a similar type-I ELM discharge. This oscillation is also seen by magnetic pick-up probes that display a strong ballooning character and $n = +1$ toroidal mode number and could help explain the markedly different pedestal dynamics observed in the small-ELM regime.

5.2. QH-mode

Some effort was dedicated to the development of a low-density H-mode scenario with counter-injected NBI heating in pursuit of conditions compatible with QH-mode. These conditions are prone to high fast ion losses yielding low ion temperatures and diminished toroidal rotation profiles. Reducing the plasma

size and, thereby, increasing the outer gap between plasma and wall, proved effective in partially restoring efficient heating. In addition, edge ECRH deposition was used to lower the density by increasing the ELM frequency. However, true quiescent conditions remain to be obtained.

5.3. Negative triangularity

Negative triangularity (NT), pioneered by TCV since the 1990s [61, 62] and recently also demonstrated in DIII-D [63], emerges as an attractive alternative scenario with H-mode like energy confinement, but with L-mode like pressure profiles and no ELMs. NT was extensively revisited taking advantage of new TCV capabilities in order to confirm an advantageous L-mode confinement and further explore its stability and exhaust properties [64].

5.3.1. Core confinement. The attractiveness of the NT tokamak arises from its advantageous confinement properties. The confinement improvement observed in limited Ohmic plasma with increasing negative triangularity has been documented up to $\delta = -0.6$ without any evidence of saturation [64].

NBI heating has permitted an extension of TCV's NT research towards more reactor-relevant regimes with $T_e/T_i \sim 1$ at low collisionality. Using NBI and ECH to scan negative triangularity in limited configurations is seen to improve confinement over the entire range of temperature ratios, T_e/T_i, from 0.5 to 5 and collisionality, $1/\nu_{\text{eff}}$, from 0.1 to 2 [65]. The correlation electron cyclotron emission diagnostic, sensitive to wavenumbers $k_\theta < 0.4\,\text{cm}^{-1}$ and measuring at $\sim 2/3$ of the minor radius ($0.55 < \rho_{\text{vol}} < 0.75$), shows a decrease in radiative temperature fluctuations, figure 9. This decrease also occurs for matched heating powers as well as for matched plasma profiles. Linear gyrokinetic flux tube simulations confirm that the turbulence regime changes from pure trapped electron mode (TEM) dominated in Ohmic and EC heated to a mixture of TEM and ion temperature gradient (ITG) modes in strongly NBI heated discharges. The simulations suggest that in both turbulence regimes, NT partially stabilises the most unstable modes with low wavenumbers and supports the idea that the critical gradients, beyond which micro-instabilities are triggered, are higher.

The investigation of NT confinement has also been extended to diverted configurations, with the port protection tiles installed throughout the 2020 campaign without baffles extending the range of possible strike point positions to the outer wall, e.g. figure 1(*e*) [64]. A scan of the upper triangularity from 0.5 to −0.5 shows a continuous improvement in the confinement time by up to 50%. Adding NBI power leads to further improvements in the $H_{98(y,2)}$ confinement factor, indicating a more favourable power and/or density dependence than in the scaling, figure 10. L–H transitions have been observed only sporadically in these fully NT diverted scenarios, indicating a wide L-mode existence range—up to 1 MW input power—despite a magnetic field directed in the traditionally favourable direction (with the ion grad B-drift directed from the core plasma towards the *X*-point).
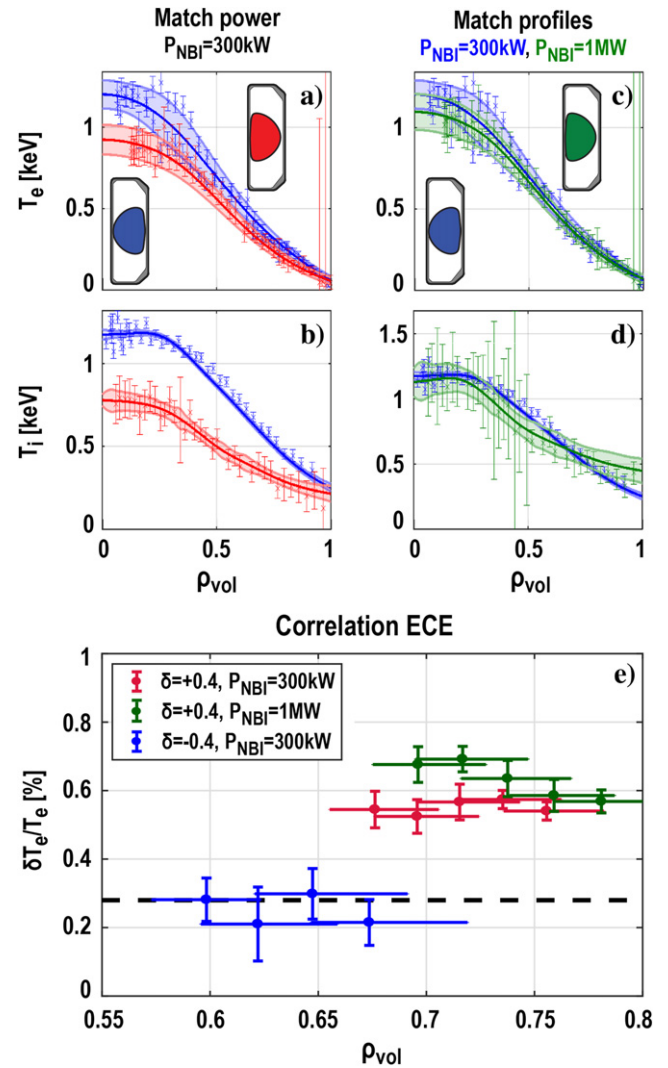

Figure 9. Comparison of positive and negative at the same heating power (*a*) and (*b*) and at the same temperatures (*c*) and (*d*), which both show a larger temperature fluctuation amplitude for $\delta > 0$ (*e*). (Adapted from [65].) Reproduced courtesy of IAEA. Figure from [65]. © 2019 EURATOM.

Understanding NT's advantageous confinement properties advanced with the first global non-linear gyrokinetic simulations using the GENE code that reproduce the observed transport level over a major portion of the minor radius for a pair of limited TCV plasmas with $\delta = -0.3$ and $\delta = +0.3$ [66]. The plasmas were heated with ECH and the turbulent transport was, consequently, in the TEM regime. In addition to predicting the absolute transport levels, the simulations also predict a density fluctuation profile as measured in similar discharges [1]. A comparison of the global calculations with local, flux tube calculations revealed that non-local effects play a crucial role in negative δ performance and must be retained to describe the experiment [66].

5.3.2. Performance. NBI heating allowed an extended operating space for NT plasmas to the ITER baseline (IBL) value of β_N (at the IBL value of q_{95}) and beyond, attaining a record β_N 3.0 [64], figure 10(*b*). However, similarly to the low-q_{95} IBL scenario in TCV, section 4.3, these discharges are prone
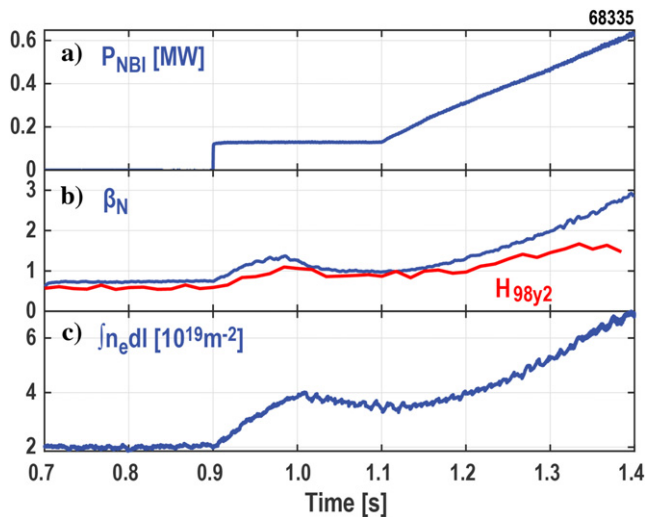
Figure 10. Diverted 220 kA NT discharge, shown in figure 1(*e*), with (*a*) NBI heating leading to (*b*) high $\beta_{\rm N}$ and good confinement quality $H_{98(y,2)}$, as well as (*c*) an increase in the density. Reproduced with permission from [64].

to NTMs, but, due to their density, are inaccessible to X2 ECH control. Instabilities have, consequently, prevented stationary conditions with strong auxiliary heating. Operational limits of NT plasmas at low q_{95} and high density are found to be similar to those for positive δ.

5.3.3. Edge. Reciprocating probe plunges past the LCFS of Ohmic, inner wall limited NT plasmas confirm a reduced turbulent radial particle flux extending from the core into the plasma edge. The reduction near the LCFS is poorly explained by reduced fluctuation amplitudes, but more by a change in the phase shift between density and potential fluctuations [64]. The saturation current is, however, dramatically reduced in the SOL region past the separatrix, which enters the vessel in sufficiently negative δ plasmas [68]. This transition is also seen clearly by the new mid-plane GPI system as a strong reduction of the fluctuation level [68], figure 11. This reduction outside the separatrix occurs equally in inner-wall limited and diverted NT plasmas. The appearance of a separatrix in the vessel, at sufficiently negative δ, also coincides with a strong decrease in the main chamber–wall interaction [68]. The decrease in fluctuation level correlates particularly well with a significant reduction in connection length of the flux tubes that connect to the outer wall. This strong decrease in main chamber PWI addresses a key concern for reactors.

With ELMs avoided and main PWI strongly suppressed, power exhaust in NT still requires mitigation of target heat fluxes. With an L-mode SOL width, though narrower than for positive δ [69] that is comparable to conventional H-modes, a reactor will have to dissipate similar levels of power in an SOL. This dissipation must be achieved along field lines that are typically shorter but end at higher target radii. Nitrogen seeding effectively decreased the plasma temperature at the outer target below 5 eV, albeit with some degradation in core confinement.

6. ITER physics/operational limits

TCV addresses critical aspects of the discharge initiation and evolution including those that may limit plasma performance or even pose a danger to the machine in ITER and future power plants.

6.1. ECR plasmas for start-up and wall conditioning

Start up in helium (He) has been investigated by comparing the 1D reaction–diffusion–convection code TOMATOR-1D to magnetised RF He plasmas in TCV [70]. Plasmas were generated and maintained with X2 heating. The model can describe the evolving density profile and reveals a decrease of the EC absorption efficiency with heating power, which is explained by electron energy gains beyond optimal for electron impact ionisation. Further experiments reveal a dramatic increase of the EC absorption efficiency when an additional vertical field in the range of 0.25%–0.5% of the toroidal field strength is applied that may result from an effective decrease in the power density at the resonance layer.

6.2. Electron cyclotron current drive

In ITER, electron cyclotron current drive (ECCD) is selected as the main tool to stabilise NTMs. Modelling, however, generally overestimates the current drive efficiency and must invoke an empirical, anomalous, transport of fast electrons to match experiments. New insight was gained by measuring the dynamic response to modulated ECCD applied at the second harmonic X-mode (X2) with an absolutely calibrated multi-chord hard x-ray spectrometer diagnostic (HXRS) [71, 72]. The applied square wave envelope with 750 kW of EC power, a modulation frequency of ∼100 Hz and duty-cycle of ∼20% is a trade-off between minimising perturbations of the equilibrium current profile and generating sufficient HXRS signal. The response to on- and off-axis ECCD, which indicates an outward transport in space and an acceleration to higher energies with time, can be compared to predictions of the time-varying Fokker–Planck modelling with the 3D bounce-averaged relativistic code LUKE coupled with the synthetic hard-x-ray diagnostic module R5-X2. Diffusivity models that depend on power (as a proxy for temperature) and/or electron momentum (as required to describe kinetic instabilities) provided significantly better agreement than a constant anomalous diffusivity, but still fell short of describing all aspects of the measured dynamic response [72]. Potential mechanisms that are being investigated include EC wave scattering by edge fluctuations, already reported in simple magnetised plasmas [73], and in dedicated experiments on TCV [74].

6.3. Neoclassical tearing modes

The ITER baseline scenario is prone to NTMs and, hence, their control is a prerequisite for safe, high performance, operation. Systematic variations of the current profile using ECCD revealed an unexpected density dependence of the onset of trigger-less NTMs. A newly developed model of the classical
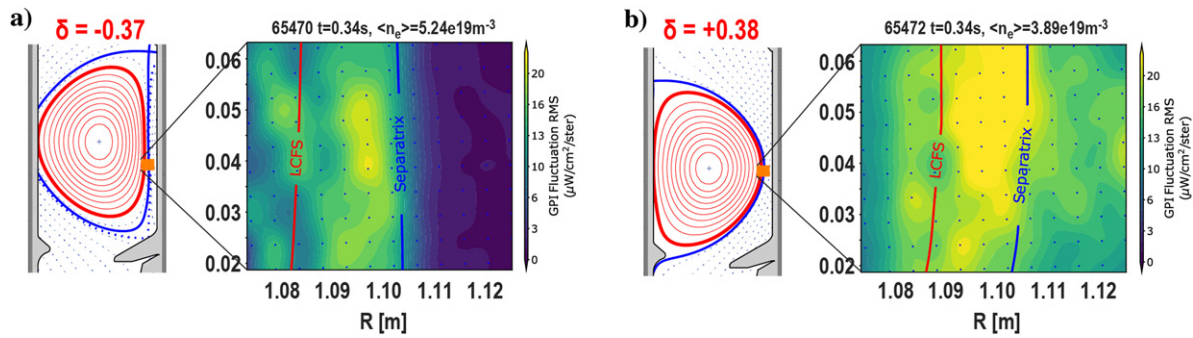
Figure 11. Fluctuation RMS of GPI measurements averaged over a 10 ms window in inner-wall limited negative (*a*) and positive (*b*) triangularity plasmas. Reproduced courtesy of IAEA. Figure from [68]. Copyright (2021) IAEA.

stability index Δ' explains these observations with the known density dependence of the current drive efficiency and a new density dependence in the stability of Ohmic plasmas that become more unstable at higher densities [75]. The improved description of the island is still sufficiently simple to be evaluated in real-time and may be used to inform the supervisory controller of an integrated control framework, such as that presented in section 7.4, of the plasma state and, thereby, facilitate NTM pre-emption in future devices.

6.4. Fast ion studies

Fast ion confinement affects the NBI and ultimately the alpha-heating in ITER. Magneto-hydrodynamic modes, some driven by the fast particle population itself, can decrease that confinement by an order of magnitude. In addition to a degradation in the auxiliary and internal heating performance, the lost, highly energetic particles can also damage the walls. It is, therefore, essential to minimise fast particle losses in safe and efficient fusion operation.

Enabled by the first NBI heating system installed in 2015, fast-ion studies are gaining prominence with the development of robust scenarios that display rich, fast-ion driven, MHD spectra [76]. Several classes of Alfvén eigenmodes (TAE, EAE, RSAE) have already been identified by mode number and frequency evolution. TAEs and EAEs occur during NBI heated phases, but only with simultaneous ECRH. EGAMs were also identified but again only with ECRH. EGAMS are driven by a bump-on-tail fast ion distribution generated by strong charge exchange losses. The dependence of beam-driven modes on ECRH is explained by its effect on the slowing down time of beam ions that increases the fast ion density. For the same reason, NBI of hydrogen, with a faster slowing down times leading to a lower fast ion density, is not seen to drive these modes. Fast ion confinement in TCV appears close to neoclassical and, thus far, is unaffected by the observed modes. In addition to the beam driven modes, a continuous mode, enhanced by NBI, is also observed. Its frequency evolution is suggestive of a TAE and it is hypothesised that it may be related to an interaction with turbulence.

A newly operational fast ion loss detector (FILD) is now operational that can delineate the reciprocal effect of these modes on the fast-ion population [77]. The diagnostic features a novel double-slit design to detect fast-ion losses in plasma
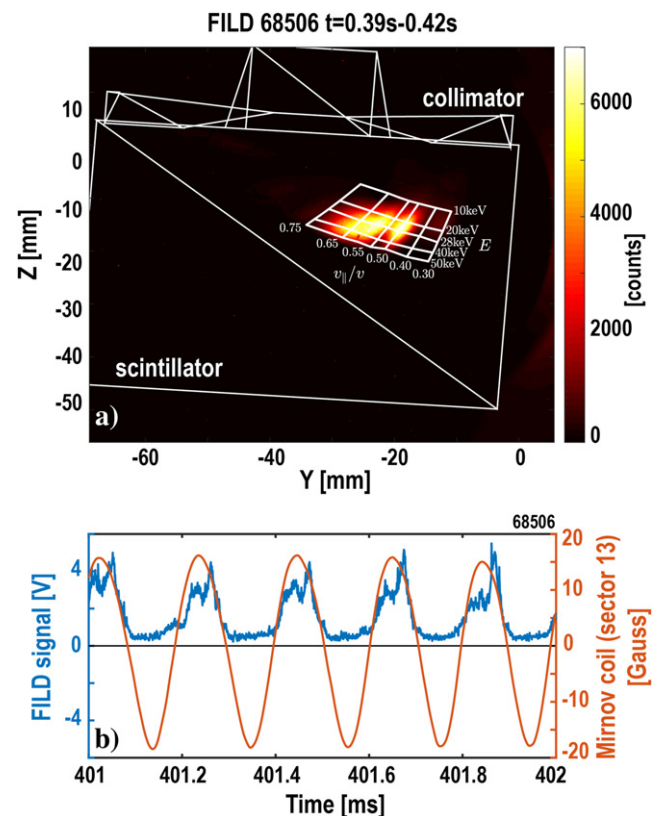

Figure 12. (*a*) Fast ion loss signal on the scintillator of the FILD averaged over 30 ms. The mapping to the particle velocity space is superimposed (white). (*b*) The average signal amplitude (blue) correlates with the local magnetic perturbation amplitude of a 2/1 NTM (orange).

discharges with either co- or counter-current injection. First measurements show, for example, an enhanced fast ion loss in NBI heated discharges with 2/1 NTMs, figure 12(*a*). The signal amplitude correlates with the maximum magnetic perturbation amplitude at the location of the FILD, figure 12(*b*).

6.5. Runaway electrons

Further experiments aim at understanding and controlling runaway electrons (REs), whether created during start-up or by disruptions, as they can cause severe damage in larger devices
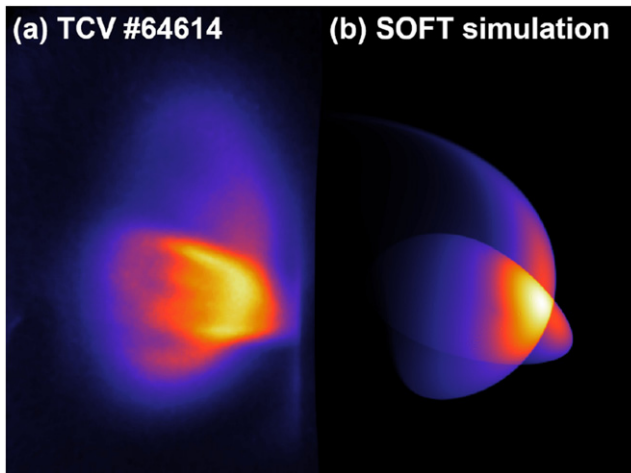
Figure 13. (*a*) Measured emission (640 nm) in discharge 64614 at $t = 0.725$ s and (*b*) corresponding synthetic image of the simulated pre-disruption RE synchrotron emission assuming $p^* = 50$ m$_e$c and $\theta^* = 0.4$ rad. Reproduced courtesy of IAEA. Figure from [79]. © 2020 EURATOM.

such as ITER. Models of RE generation, and their subsequent dynamics, must be validated through comparison with experiments. On TCV, RE beams were routinely and reproducibly created using Ne or Ar injection through a dedicated large aperture fast valve. The RE scenarios were recently extended to use He, Kr and Xe injection, and NT and diverted configurations, increasing the region available for model validation.

Filtered imaging for multiple wavelength ranges, avoiding in particular contributions from strong line radiation using TCV's MULTICAM diagnostic, provided the first measurements of synchrotron radiation emitted by an RE beam on TCV and even allowed the detection of pre-disruption seed distributions, figure 13(*a*), [78]. The versatility of TCV and its control system allowed the beam to be vertically displaced, altering the diagnostic viewing angle, and thereby test the synthetic synchrotron diagnostic SOFT, figure 13(*b*). A comparison with kinetic theory for RE dynamics in uniform magnetic fields indicates significant non-collisional pitch angle scattering as well as radial transport of REs, as can be caused by magnetic perturbations [79].

In addition, strategies to purge the impurities from a post-mitigation RE beam with secondary D_2 injection are being explored. He, Ne and Ar have been successfully purged and the required D_2 density scanned. Mitigation with pure D_2 injection, however, led to a full RE current re-conversion and subsequent return to a thermal plasma within 50 ms [80].

7. Development of control solutions

TCV continues to explore its flexible digital control system with a growing number of measurements becoming available in real-time to enhance available control solutions. These are integrated into a generic plasma control framework to address the needs of next-generation tokamaks [81].

7.1. Plasma start-up control

A new procedure to calculate the PF coil current trajectories during plasma start-up was applied to the development of doublet-shaped plasmas, which feature two magnetic axes and an internal separatrix. Following encouraging results obtained in 2017 [82], new experiments were performed that attempted to obtain stationary doublet plasmas lasting many current redistribution times. The new procedure achieved reliable and reproducible breakdowns and early ramp-up with two separate current channels. Depending upon the programed PF coil trajectories, the two current channels could be made to either part into separate droplets, or merge into a single-axis plasma. This experimental campaign yielded valuable data on the early formation of doublets providing the validation of new and promising control tools, to be tested further in future campaigns.

7.2. Plasma exhaust control

Plasma exhaust control, for future reactors, was explored using an estimate of the CIII radiation profile along the divertor leg, indicative of the local T_e, as a proxy for detachment. The strategy comprised real-time-analysis of spectral video images using the MANTIS diagnostic [83], experiments to characterise the dynamic relationship between gas valve actuation and displacement of the emission front [84] and offline feedback design and resulted in the demonstration of feedback control of the distance of the radiation from the target to the X-point for both L- and H-mode scenarios [85].

7.3. Real-time plasma state detection

An important requirement for integrated real-time control is to know the state of the plasma.

7.3.1. Confinement states. In particular the confinement mode is a key quantity to be known, as, for example, unexpected H–L back transitions can often indicate proximity to an imminent density limit disruption, section 4.4. Confinement mode transitions are often easily distinguished by human operators correlating visible light signals with line-integrated density measurements. To automate this, several deep-learning based confinement state detectors were implemented and tested on TCV data [86–88]. The detectors are able to distinguish between *L-mode*, *H-mode* and *dithering* states with high fidelity when verified against human-labelled data. These detectors are being further improved and prepared for implementation into TCV's plasma control system.

7.3.2. Kinetic equilibrium reconstruction. Knowledge of the flux distribution and internal plasma profiles is essential for many control tasks in fusion plasmas. Plasma equilibria on TCV are routinely reconstructed in real-time using readily available magnetic measurements. These equilibrium reconstructions can be improved by constraining the plasma current or pressure profiles with measurements or (dynamic) modelling, a technique usually referred to as *kinetic equilibrium reconstructions* or *integrated data analysis*. Kinetic

equilibrium reconstructions, based on dynamic modelling have, now, for the first time, been carried out in real-time by coupling the free-boundary equilibrium code LIUQE with the 1.5D transport code RAPTOR, during TCV discharges [89]. In addition to the magnetic measurements, the equilibrium is also constrained by estimates of pressure and current density profiles from real-time evolution of the 1D transport equations, which are, in turn, constrained by measurements of the line integrated density obtained from the interferometer and a central electron temperature obtained from differentially filtered SXR diodes. Running the algorithm on a single node of the control system achieves a cycle time of less than 1.6 ms, which is faster than the current diffusion and energy confinement times and, therefore, sufficient to track changes in the internal profiles.

7.4. Generic control framework

With a view to future long-pulse tokamak discharges, a generic and, therefore, easily transferable plasma control framework has been developed and implemented in the TCV control system [90, 91]. Such a control framework includes real-time plasma state reconstruction, monitoring and supervision, and actuator management, as well as robust detection and handling of off-normal events. The novel framework consists of a tokamak-specific *interface layer* and a tokamak-independent *task layer*. The interface layer translates diagnostic and actuator signals into general descriptions of the state of the plasma and the actuators that can be processed by the task layer. Real-time decisions on control task priorities are taken by a high-level supervisory controller based on the detection of off-normal events, with details in the task execution delegated to lower-level, multiple, controllers. This plasma control framework was tested in numerous TCV experiments. The first example demonstrated real-time re-assignment of ECRH actuators from q-profile and β_N control to NTM control in response to the appearance of a mode [91, 92]. More recently, a density limit disruption avoidance algorithm was implemented within the same framework (see section 4.4). This algorithm controls the NBI power and the fuelling rate based upon a real-time estimated proximity to the disruptive boundary [93], previously identified on ASDEX Upgrade [94].

8. Conclusions

Despite a major TCV opening to instal new divertor baffles in 2019 and adverse boundary conditions dictated by the global health crisis that started to unfold in early 2020, the TCV tokamak has remained highly productive. The scientific programme continues to balance focussed research towards the success of ITER and the development of a DEMO through a close integration within the European fusion programme, whilst retaining the academic curiosity to develop solutions and allow for scientific discoveries. The addition of gas baffles for a dedicated campaign in 2019 and further campaigns planned demonstrated yet another dimension in TCV's signature flexibility. The associated experiments are an integral part of the European strategy to address the exhaust issue in

a future reactor through proof of principle experiments, such as the super-X divertor, and model validation, for example, as started with SOLPS-ITER. The model validation effort, in particular, is gaining prominence as edge turbulence codes such as GBS can now simulate the entire TCV edge plasma with realistic parameters [95]. In parallel, drift-kinetic and gyrokinetic models of the plasma edge are being developed to overcome the limitations of fluid codes [96, 97]. The increased heating capabilities broaden the operational regime with $T_e/T_i \sim 1$ and have stimulated a general shift from L-mode towards more H-mode studies, where ITER baseline parameters were reached in type-I ELMy H-modes, power dissipation in the baffled divertor increased in scenarios with higher q_{95} and alternative regimes with 'small', or no, ELMs explored. A significant effort was dedicated to confirming negative triangularity as an attractive scenario with L-mode confinement matching that of H-modes for positive triangularity without harmful ELMs and a strongly reduced PWI in the main chamber. Finally, the control effort has extended its scope from devising novel real-time-observers, such a kinetic equilibrium reconstructions and impurity emission front location estimates and demonstrating control solutions, such as detachment control, to developing and testing a general framework that will be needed for future devices.

Further versions of baffles will be tested in 2021 and 2022, initially focussing on snowflake configurations. In the short term, TCV's heating capability will also be enhanced by a second NBI system, operating with energies up to 60 keV. This beam's orientation is the reverse of the existing beam allowing the independent control of heating power and torque. The higher beam energy will also greatly enhance the operating space for fast ion studies. In the medium term, further increases of the power and flexibility of the EC system, with additional dual frequency gyrotron at MW levels are foreseen. It is also envisaged to employ the now proven technique of machined tiles to test a specific alternative divertor configuration including optimised target geometries, with a 'long-legged, tightly baffled' geometry identified as a potential game changing concept.

ORCID iDs

H. Reimerdes https://orcid.org/0000-0002-9726-1519

References

[1] Hofmann F. *et al* 1994 *Plasma Phys. Control. Fusion* **36** B277

[2] Fasoli A. *et al* 2020 *Nucl. Fusion* **60** 016019
[3] Zohm H., Militello F., Morgan T.W., Morris W., Reimerdes H. and Siccinio M. 2021 *Fusion Eng. Des.* **166** 112307
[4] Karpushov A.N. *et al* 2017 *Fusion Eng. Des.* **123** 468
[5] Sorokin A. *et al* 2020 *Rev. Sci. Instrum.* **91** 013323
[6] Toussaint M., Coda S., Dolizy F., Duval B., Karpushov A.N., Martin Y. and Maurizio R. and the TCV Team 2020 *Fusion Eng. Des.* **155** 111695
[7] Alberti S. *et al* 2019 High-efficiency, long-pulse operation of MW-level dual-frequency gyrotron, 84/126 GHz, for the TCV tokamak *44th Int. Conf. Infrared, Millimeter, and Terahertz Waves (Irmmw-Thz)* (Paris, France, 1–6 September 2019)
[8] Hogge J.-P. *et al* 2020 *AIP Conf. Proc.* **2254** 090006
[9] Reimerdes H. *et al* 2021 *Nucl. Fusion* **61** 024002
[10] De Oliveira H., Marmillod P., Theiler C., Chavan R., Février O., Labit B., Lavanchy P., Marlétaz B. and Pitts R.A. and the TCV Team 2019 *Rev. Sci. Instrum.* **90** 083502
[11] De Oliveira H., Theiler C. and Elaian H. and the TCV Team 2021 *Rev. Sci. Instrum.* **92** 043547
[12] Arnichand H. *et al* 2019 *J. Instrum.* **14** C09013
[13] Perek A. *et al* 2019 *Rev. Sci. Instrum.* **90** 123514
[14] Martinelli L. *et al* 2021 Spectroscopic studies of TCV divertor plasma with the DSS upgrade *47th EPS Conf. Plasma Physics, Europhysics Conf. Abstract* (21–25 June 2021) (virtual conference) vol 45A (http://ocs.ciemat.es/EPS2021PAP/pdf/O5.J502.pdf)
[15] Wensing M. *et al* 2019 *Plasma Phys. Control. Fusion* **61** 085029
[16] Février O. *et al* 2021 *Nucl. Mater. Energy* **27** 100977
[17] Wensing M. 2021 Drift-related transport and plasma–neutral interaction in the TCV divertor *PhD Thesis* EPFL No. 8447 (https://doi.org/10.5075/epfl-thesis-8447)
[18] Galassi D. *et al* 2020 *Plasma Phys. Control. Fusion* **62** 115009
[19] Pitts R.A. *et al* 2019 *Nucl. Mater. Energy* **20** 100696
[20] Reimerdes H. *et al* 2020 *Nucl. Fusion* **60** 066030
[21] Militello F. *et al* 2021 *Nucl. Mater. Energy* **26** 100908
[22] De Oliveira H. 2021 A fast-moving Langmuir probe array for the divertor of the tokamak à configuration variable *PhD Thesis* EPFL No. 8407 (https://doi.org/10.5075/epfl-thesis-8407)
[23] Wensing M., Loizu J., Reimerdes H., Duval B.P. and Wischmeier M. and the TCV Team 2020 *Nucl. Fusion* **60** 054005
[24] Wensing M. *et al* 2020 *Nucl. Mater. Energy* **25** 100839
[25] Wensing M. *et al* 2021 *Phys. Plasmas* **28** 082508
[26] Verhaegh K. *et al* 2021 *Plasma Phys. Control. Fusion* **63** 035018
[27] Verhaegh K. *et al* 2021 *Nucl. Mater. Energy* **26** 100922
[28] Février O. *et al* 2020 *Plasma Phys. Control. Fusion* **62** 035017
[29] Smolders A. *et al* 2020 *Plasma Phys. Control. Fusion* **62** 125006
[30] Harrison J. *et al* 2021 Overview of first physics results from MAST Upgrade *2020 IAEA Fusion Energy Conf. (virtual conference)* (10–15 May 2021) p EX/P6-39
[31] Fil A. *et al* 2020 *Plasma Phys. Control. Fusion* **62** 035008
[32] Theiler C. *et al* 2021 Advances in understanding power exhaust physics with the new, baffled TCV divertor *2020 IAEA Fusion Energy Conf. (virtual conference)* (10–15 May 2021) p EX/P7-5
[33] Maurizio R. *et al* 2019 *Nucl. Fusion* **59** 016014
[34] Tsui C.K. *et al* 2021 *Nucl. Fusion* **61** 046004
[35] Gorno S. *et al* 2021 Effect of baffles on the N2-seeded snowflake minus low-field side configuration in the tokamak à configuration variable (TCV) *47th EPS Conf. Plasma Physics, Europhysics Conf. Abstract (virtual conference)* vol 45A (21–25 June 2021) (http://ocs.ciemat.es/EPS2021PAP/pdf/P3.1024.pdf)
[36] Maurizio R. *et al* 2018 *Nucl. Fusion* **58** 016052
[37] Horacek J. *et al* 2020 *Nucl. Fusion* **60** 066016
[38] Giacomin M., Stagni A., Ricci P., Boedo J.A., Horacek J., Reimerdes H. and Tsui C.K. 2021 *Nucl. Fusion* **61** 076002

[39] Riva F., Lanti E., Jolliet S. and Ricci P. 2017 *Plasma Phys. Control. Fusion* **59** 035001
[40] Riva F., Tsui C.K., Boedo J.A. and Ricci P. 2020 *Phys. Plasmas* **27** 012301
[41] Scarabosio A., Eich T., Herrmann A. and Sieglin B. 2013 *J. Nucl. Mater.* **438** S426
[42] Maurizio R., Duval B.P., Labit B., Reimerdes H., Faitsch M., Komm M., Sheikh U. and Theiler C., the TCV Team and the EUROfusion MST1 Team 2021 *Nucl. Fusion* **61** 024003
[43] Eich T. *et al* 2013 *Nucl. Fusion* **53** 093031
[44] Tsui C. *et al* 2021 Density shoulder dependence on divertor closure and main-chamber neutral pressure *Nucl. Fusion* (submitted)
[45] Zhang Y. and Krasheninnikov S.I. 2020 *Plasma Phys. Control. Fusion* **62** 115018
[46] Thrysøe A.S. *et al* 2020 *Phys. Plasmas* **27** 052302
[47] Vianello N. *et al* 2021 SOL profile and fluctuations in different divertor recycling conditions in H-mode plasmas *2020 IAEA Fusion Energy Conf. (virtual conference)* (10–15 May 2021)
[48] Labit B. *et al* 2021 H-mode power threshold experiments in mixed ion species plasmas on TCV *25th Joint EU-US Transport Task Force Meeting*
[49] Martin Y.R. and Takizuka T. (The ITPA CDBM H-mode Threshold Data Group) 2008 *J. Phys.: Conf. Ser.* **123** 012033
[50] Sheikh U.A. *et al* 2019 *Plasma Phys. Control. Fusion* **61** 014002
[51] Sheikh U.A. *et al* 2021 *Nucl. Mater. Energy* **26** 100933
[52] Sauter O. *et al* 2021 ITER baseline scenario investigations on the TCV tokamak and comparison with AUG *2020 IAEA Fusion Energy Conf. (virtual conference)* (10–15 May 2021) p EX/P4-18
[53] Bernert M. *et al* 2015 *Plasma Phys. Control. Fusion* **57** 014038
[54] Pau A. *et al* 2020 Active disruption avoidance for H-mode density limits on TCV and ASDEX Upgrade *Poster Presented at 31st Symp. Fusion Technology (SOFT 2020)* (20–25 Sept. 2020) virtual edition
[55] Labit B. *et al* 2019 *Nucl. Fusion* **59** 086020
[56] Faitsch M., Eich T., Harrer G.F., Wolfrum E., Brida D., David P., Griener M. and Stroth U., the ASDEX Upgrade Team and the EUROfusion MST1 Team 2021 *Nucl. Mater. Energy* **26** 100890
[57] Labit B. *et al* 2021 H-mode physics studies on TCV supported by the EUROfusion pedestal database *2020 IAEA Fusion Energy Conf. (virtual conference)* (10–15 May 2021) p EX/P4-17
[58] Faitsch M. *et al* 2021 High density, high confinement, power exhaust compatible H-mode regime in TCV and ASDEX Upgrade *2020 IAEA Fusion Energy Conf. (virtual conference)* (10–15 May 2021) p EX/P4-20
[59] Molina Cabrera P.A., Labit B., Coda S. and Porte L. and the TCV Team 2021 *Plasma Phys. Control. Fusion* **63** 085019
[60] Molina Cabrera P., Coda S., Porte L. and Smolders A. and the TCV Team 2019 *Rev. Sci. Instrum.* **90** 123501
[61] Pochelon A. *et al* 1999 *Nucl. Fusion* **39** 1807
[62] Camenen Y. *et al* 2007 *Nucl. Fusion* **47** 510
[63] Austin M.E. *et al* 2019 *Phys. Rev. Lett.* **122** 115001
[64] Porte L. *et al* 2021 The route to high performance, DEMO relevant, negative triangularity tokamak operation on TCV *2020 IAEA Fusion Energy Conf. (virtual conference)* (10–15 May 2021) p EX/P6-RB
[65] Fontana M., Porte L., Coda S., Sauter O., Brunner S., Jayalekshmi A.C., Fasoli A. and Merlo G. and the TCV Team 2020 *Nucl. Fusion* **60** 016006
[66] Merlo G. *et al* 2021 *Plasma Phys. Control. Fusion* **63** 044001
[67] Huang Z. and Coda S. and the TCV Team 2019 *Plasma Phys. Control. Fusion* **61** 014021

[68] Han W., Offeddu N., Golfinopoulos T., Theiler C., Tsui C.K., Boedo J.A. and Marmar E.S. and the TCV Team 2021 *Nucl. Fusion* **61** 034003

[69] Faitsch M. *et al* 2018 *Plasma Phys. Control. Fusion* **60** 045010

[70] Wauters T. *et al* 2020 *Plasma Phys. Control. Fusion* **62** 105010

[71] Choi D., Coda S., Decker J. and Peysson Y. and the TCV Team 2020 *Fusion Eng. Des.* **159** 111733

[72] Choi D., Coda S., Decker J., Cazabonne J.A. and Peysson Y. and the TCV Team 2020 *Plasma Phys. Control. Fusion* **62** 115012

[73] Chellaï O. *et al* 2018 *Phys. Rev. Lett.* **120** 105001

[74] Chellaï O. *et al* 2021 *Nucl. Fusion* **61** 066011

[75] Kong M., Sauter O., Felici F., Hogeweij G.M.D., Merle A. and Nowak S. and the TCV Team 2020 *Nucl. Fusion* **60** 026002

[76] Geiger B. *et al* 2020 *Plasma Phys. Control. Fusion* **62** 095017

[77] Stipani L. 2021 A fast ion loss detector for the TCV tokamak *PhD Thesis* EPFL No. 8327 (https://doi.org/10.5075/epfl-thesis-8327)

[78] WijkampP T.A. *et al* 2021 *Nucl. Fusion* **61** 046044

[79] Hoppe M. *et al* 2020 *Nucl. Fusion* **60** 094002

[80] Sheikh U.A. *et al* 2020 Runaway electron studies and plasma restart from a RE beam on TCV *IAEA Technical Meeting on Plasma Disruptions and their Mitigation (Virtual Meeting)* (20–23 July 2020) pp 20–3

[81] Felici F. 2021 Integrated plasma state reconstruction, off-normal event handling and control, with application to TCV and ASDEX Upgrade *IAEA Fusion Energy Conf. (Virtual Conference)* (10–15 May 2021) p EX/P421

[82] Duval B.P. *et al* 2018 Singlet breakdown optimization to a doublet plasma configuration on the TCV tokamak *2018 IAEA Fusion Energy Conf.* (Gandhinagar, India, 22–27 Oct. 2018) p EX/P1-6

[83] Ravensbergen T. *et al* 2020 *Nucl. Fusion* **60** 066017

[84] Van berkel M. *et al* 2020 *Plasma Phys. Control. Fusion* **62** 094001

[85] Ravensbergen T. *et al* 2021 *Nat. Commun.* **12** 1105

[86] Matos F., Menkovski V., Felici F., Pau A. and Jenko F., the TCV Team and the EUROfusion MST1 Team 2020 *Nucl. Fusion* **60** 036022

[87] Marceca G. *et al* 2020 Detection of plasma confinement states in the TCV tokamak *Workshop at the 34th Conf. Neural Information Processing Systems (NeurIPS)* (11 December 2020) virtual event (https://ml4physicalsciences.github.io/2020/files/NeurIPS_ML4PS_2020_44.pdf)

[88] Matos F., Menkovski V., Pau A., Marceca G. and Jenko F. and the TCV Team 2021 *Nucl. Fusion* **61** 046019

[89] Carpanese F., Felici F., Galperti C., Merle A., Moret J.M. and Sauter O. and the TCV Team 2020 *Nucl. Fusion* **60** 066020

[90] Blanken T.C., Felici F., Galperti C., Vu N.M.T., Kong M., Sauter O. and de Baar M.R., the EUROfusion MST1 Team and the TCV Team 2019 *Nucl. Fusion* **59** 026017

[91] Vu N.M.T., Blanken T.C., Felici F., Galperti C., Kong M., Maljaars E. and Sauter O., the TCV Team and the EUROfusion MST1 Team 2019 *Fusion Eng. Des.* **147** 111260

[92] Kong M. *et al* 2019 *Nucl. Fusion* **59** 076035

[93] Vu T., Felici F., Galperti C., Maraschek M., Pau A., Rispoli N., Sauter O. and Sieglin B. 2021 *IEEE Trans. Nucl. Sci.* **68** 1855

[94] Maraschek M. *et al* 2018 *Plasma Phys. Control. Fusion* **60** 014047

[95] Giacomin M. and Ricci P. 2020 *J. Plasma Phys.* **86** 905860502

[96] Jorge R., Ricci P. and Loureiro N.F. 2017 *J. Plasma Phys.* **83** 905830606

[97] Frei B.J., Jorge R. and Ricci P. 2020 *J. Plasma Phys.* **86** 905860205